

Integrated relay server for measurement-device-independent quantum key distribution

Peiyu Zhang^{1,†}, Xiaodong Zheng^{1,†}, Renyou Ge^{2,†}, Liangliang Lu^{1,†}, Qi Chen^{1,†}, Fangchao Qu¹,
Labao Zhang^{1,*}, Xinlun Cai^{2,*}, Yanqing Lu¹, Shining Zhu¹, Peiheng Wu¹, Xiao-Song Ma^{1,*}

¹ National Laboratory of Solid-State Microstructures,
Collaborative Innovation Center of Advanced Microstructures,
School of Physics, Research Institute of Superconducting Electronics,
School of Electronic Science and Engineering,
Nanjing University, Nanjing 210093, China

² State Key Laboratory of Optoelectronic Materials and Technologies,
School of Electronics and Information Technology,
Sun Yat-sen University, Guangzhou 510000, China

[†]These authors contributed equally to this work

*e-mails: lzhang@nju.edu.cn; caixlun5@mail.sysu.edu.cn; xiaosong.ma@nju.edu.cn

(Dated: May 7, 2022)

Quantum key distribution (QKD) promises security stemming from the laws of quantum physics. QKD devices based on integrated chips not only provides miniaturization, but also enhanced performance, which is important to practical and scalable networks. Here we report the realization of a relay server for measurement-device-independent QKD based on a heterogeneous superconducting-silicon-photonics chip. Silicon waveguides and beam splitters are used for optical guidance and interference. Waveguide integrated superconducting nanowire single-photon detectors are used to detect single photons. We show Hong-Ou-Mandel interference between weak coherent states with a visibility of $48\% \pm 2\%$. Our system generates 733 sifted bits at about 71 dB attenuation (equivalent to 358 km standard fiber) with a quantum bit error rate of $3.5\% \pm 0.7\%$. The fabrication processes of our device are compatible with standard thin-film technology. Together with integrated QKD transmitters, a scalable, chip-based and cost-effective QKD network can be realized in the near future.

QKD employs the laws of quantum physics and promises information-theoretical security for key exchange [1–4]. Despite the tremendous progress in the last 35 years, practical implementations of QKD still deviate from ideal description in security proofs due to potential side-channel attacks. For instance, a series of loopholes have been identified due to the imperfections of measurement devices [5–8]. Inspired by the time-reversed entanglement-based QKD, measurement-device-independent QKD (MDI-QKD), which removes all detector side attacks, has been proposed [9]. Instead of relying on the trusted nodes in the traditional QKD protocols, MDI-QKD only requires a central node (Charlie) to perform Bell-state measurement (BSM). The entanglement-like correlations between the two senders (Alice and Bob) can be obtained from BSM results. Importantly, even if Charlie is untrusted, one can still guarantee the security of the MDI-QKD as long as Charlie can project his two photons onto Bell states. The outstanding features of MDI-QKD invited global experimental efforts, which are mainly based on bulk/fiber components [10–18]. Despite the new additional BSM by Charlie, the key rate [15] and the communication distance [16] of MDI-QKD can be comparable with those of traditional QKD. Furthermore, the topology of MDI-QKD quantum networks is star-like and is naturally suitable for the metropolitan networks with multiple users [19–21].

From the perspectives of hardware, integrated photonic devices have recently been employed in QKD, in which on-chip encoders based on silicon modulators [22–25], on-chip transmitters including laser, photodiodes, modulators based on indium phosphide (InP) and decoders based on silicon oxynitride [26] and silicon dioxide [27]. Integrated silicon photonic chips for continuous-variable quantum key distribution have also been reported [28] have been shown. Most of the components used in QKD, including lasers, modulators and passive components (beam splitters, attenuators and so on) are widely used in classical optical communication systems and are not specifically designed for QKD. However, single-photon detectors are unique and are quintessential for QKD, because the security of QKD relies on single-photon detection. Senders pulses with a mean photon number must be less than 1. This particular requirement impedes the use of strong-light detectors in QKD. To the best of our knowledge, this most important component/equipment in QKD system, the single-photon detector, has not been integrated onto a chip platform and employed in a QKD system. In this work, we report the realization of a heterogeneous superconducting-silicon-photonics chip and the application of it in an MDI-QKD experiment.

Our scheme is shown in Fig. 1. Modulated weak coherent pulses are prepared by Alices (A_1, A_2, \dots, A_n) and Bobs (B_1, B_2, \dots, B_n), and are sent to the routers. Two routers select the pair of the communicating Alice and Bob, and send their pulses to an untrusted relay server controlled by Charlie. At Charlies station, a chip with heterogeneous superconducting-silicon-photonics circuitries is used. On this chip, silicon waveguides and beam splitters are used for optical guidance and interference. Waveguide integrated superconducting nanowire single-photon detectors (SNSPDs) are used to detect single photons. A single chip with multiple low-dead time (hence high-repetition-rate) [29], low-jitter [30] and high-detection efficiency detectors in conjunction with low-loss silicon photonics are intrinsically suitable for large-scale star-like MDI-QKD network [31].

Here, to the best of our knowledge, we report the first demonstration of MDI-QKD with a relay server based on an integrated

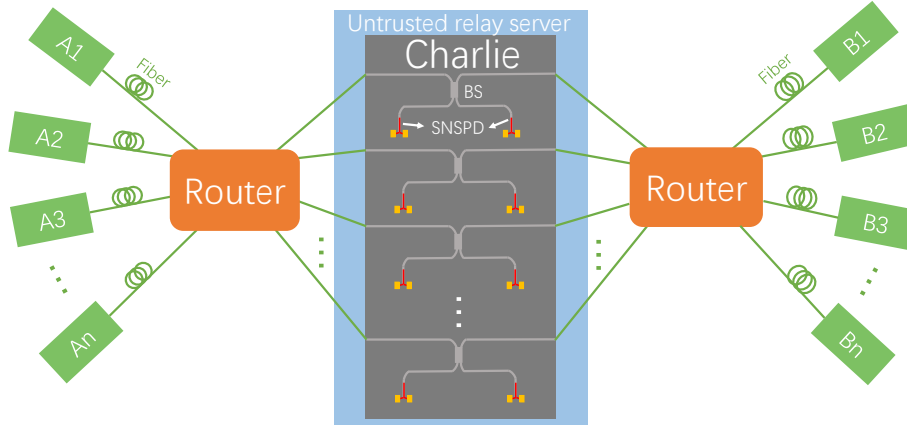


FIG. 1: **Schematic of a star-like MDI-QKD network.** A series of Alice (A_1, A_2, \dots, A_n) and Bob (B_1, B_2, \dots, B_n) prepare modulated weak coherent pulses and send to the routers. Two routers select a pair of Alice and Bob and send their pulses to an untrusted relay server controlled by Charlie. In this work, we use a silicon chip with heterogeneous superconducting-photonic circuits to realize the relay server, which consists of arrays of waveguide-based beam splitters and waveguide-integrated superconducting-nanowire single-photon detectors (SNSPDs).

chip. We expect that the fully integrated MDI-QKD network can be achieved by combining recently demonstrated transmitter chip [32, 33], benefiting low-cost and scalable secure metropolitan communications.

We implement the time-bin encoded MDI-QKD. The schematic of the experimental setup is shown in Fig.2 (a). One of the most important requirements of MDI-QKD is to obtain high-quality two-photon Hong-Ou-Mandel (HOM) interference on the integrated relay serve. To achieve that, it is necessary for Alice and Bob to generate indistinguishable weak-coherent pulses. The interfering pulses have to be indistinguishable in all degrees of freedom (DOF), including spectrum, timing, and polarization. For spectrum DOF, Alice and Bob's unmodulated pulses pass through polarization beam splitters (PBSs), and with one of the outputs connected with a 50:50 beam splitter (BS) for frequency beating. From the beating signal, we feedback onto one of the lasers and regulate the wavelength difference of these two lasers to be within 0.1 pm . Then, Alice (Bob) chops the CW laser operated at about 1536.47 nm into desired pulse sequences. The pulse width is about 426 ps and separated by 2 ns at 100 MHz rate. Z-basis (X-basis) states are generated by chopping the laser into early or (and) late time bins with intensity modulators (IMs). The average photon numbers per pulse in the two bases are about the same. The resulting pulses are sent into phase modulator (PM) with π -phase shift is applied only for the generation of $|-\rangle$ state. The electrical signals applied to the modulators are generated by an arbitrary waveform generator (AWG). An additional 50:50 beam splitter (BS) combined with a power sensor (PS) is employed to monitor the long-term stability of laser power in each encoder.

For polarization DOF, two electrical polarization controllers (EPC) are used to optimize the polarization of both pulses before they are coupled into Charlie's Chip. For temporal DOF, we adjust the relative electrical delay between Alice's and Bob's IMs to ensure their pulses arriving at the chip simultaneously. Attenuators are used to reduce and set the average photon number per pulse to be about 0.43. Then these pulses are sent to the chip. By measuring the coincidence count between two subsequent time bins from two detectors, we project the photonic states onto singlet state, $|\Psi^-\rangle = 1/\sqrt{2}(|01\rangle - |10\rangle)$.

We employ six-step heterogeneous fabrication techniques to realize the integrated chip of the relay server. Firstly, we make gold markers for the grating couplers and SNSPDs on top of a 220 nm silicon on $3 \mu\text{m}$ thermally grown SiO_2 on Si wafers. Secondly, we expose the silicon photonics layer (including waveguides, MMIs and grating couplers) to the electron beams aligning to the gold markers in the first step. Thirdly, a SiO_2 top cladding is deposited via the Plasma-Enhanced Chemical Vapor Deposition (PECVD) and planarized by chemical mechanical polishing, resulting in an optimized thickness. Then we deposit Au back-reflected mirrors and flip-bond the chip with benzocyclobuten (BCB) to a carrier wafer and the substrate of the chip is removed by mechanical grinding and dry etching. The SiO_2 is removed partly by etching. Fourthly, we employ DC reactive magnetron sputtering to deposit a nominal 6 nm NbN film on top of the chip. Fifthly, we make the gold electrode pads with a lift-off process. And a 10 nm thick SiO_2 is deposited on to NbN layer in order to improve the adhesion [34]. Finally, nanowire detectors are fabricated by e-beam lithography and timed reactive ion etching (RIE) step using CF_4 chemistry. Note that in order to align the nanowire detectors along with silicon waveguides and electrode pads, we use the set of gold markers fabricated in the first step for the pattern markers through the whole five steps. The resulting device is shown in Fig. 2(a-c).

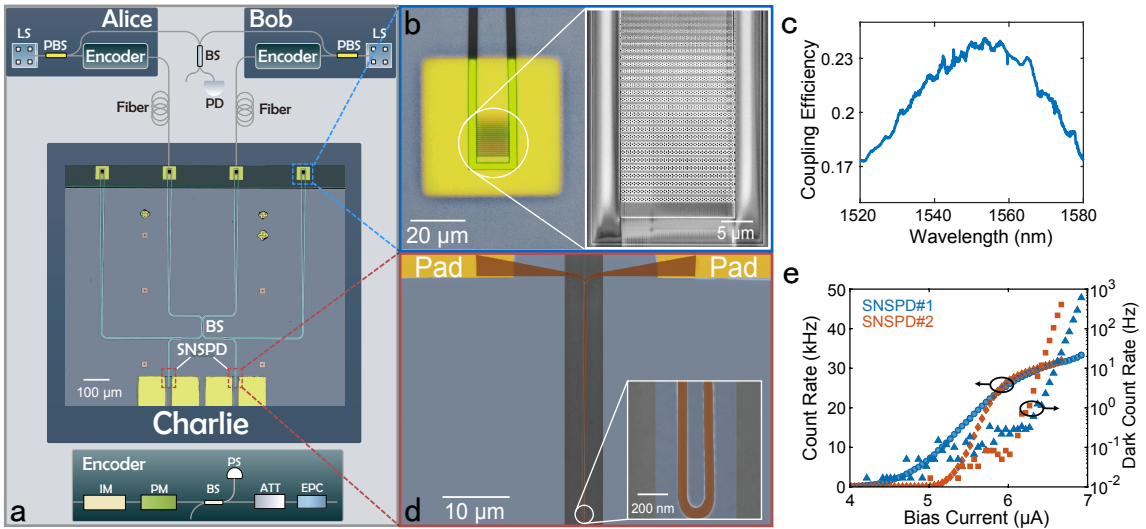


FIG. 2: Experimental devices and setup. **(a)** Schematic of experimental setup. Alice and Bob each employs a continuous wave (CW) laser (LS), and chops out early ($|0\rangle$) or/and late ($|1\rangle$) temporal modes by using intensity modulator (IM) to generate time-bin qubits with 426 ps duration and separated by 2 ns with a 100 MHz repetition rate. The phase modulators (PM) only affect the qubits in X basis, within which a π -phase is applied to the late temporal modes for $|-\rangle$ ($|0\rangle-|1\rangle$) while 0-phase for $|+\rangle$ ($|0\rangle+|1\rangle$). Variable attenuators (ATTs) are used to prepare weak coherent pulses. The pulses travel through fibers and are coupled into the integrated chip of the relay server (Charlie) for Bell-state measurement (BSM). This is enabled by a multi-mode interferometer (MMI) acting as a 50:50 beam splitter (BS) followed by two superconducting nanowire single-photon detectors (SNSPDs). **(b)** Optical and scanning electron microscopy (SEM) pictures of the high-efficiency photonic-crystal grating coupler with back-reflected mirror. **(c)** The optical transmission spectrum of the grating coupler measured with a room temperature coupling stage. **(d)** Scanning electron micrograph of the SNSPD with a 60 nm-wide, 80 μm -long U-shaped nanowire which is connected with two golden pads and integrated on 500 nm-wide silicon waveguides. Inset shows the zoomed part of the nanowire. **(e)** On-chip count rate (OCCR) and dark count rate as a function of bias current for the SNSPDs. The OCCR is measured with an input laser power of -96 dBm. It reveals that for $I_c=6 \mu\text{A}$, the dark count rate is below 0.25 Hz for the two SNSPDs. Abbreviations: PBS, polarization beam splitter; PD, photodiode; EPC, electrical polarization controller.

The integrated chip of the relay server is mounted on a nanopositioner in a closed-cycle cryostat with 2.2 K temperature (sample temperature). Fig. 2(b) shows the scanning electron microscope image of photonic crystal grating coupler [35], which is used to couple light from fiber array to the chip. The grating coupler with back-reflected mirrors provides a coupling efficiency to be more than 20% at wavelength of 1550nm, as shown in Fig. 2(c). Note that at room temperature, we have obtained over 70% coupling efficiency for particular devices, which gives us room for optimization of future devices with a six-axis coupling stages (see Supplementary Information). We employ four grating couplers, in which the two middle ones are input ports for Alice and Bob, respectively. The other two are reference ports which are used to align the fiber array with respect to the chip and calibrate coupling efficiency. There are three multi-mode interference (MMI) devices acting as a 50:50 beam splitter on the chip. The central MMI device is for two-photon interference and the subsequent two MMIs split the optical signals identically. Half of the photons are guided towards SNSPDs and the other half are guided to the reference ports. As shown in Fig. 2(d), an SNSPD is integrated on the optical waveguide. Two such waveguides integrated SNSPDs work simultaneously for detecting photons. Both SNSPDs are biased with a constant voltage source and connected with electronic readout circuitries.

We characterize the performance of our SNSPDs including on-chip counting rate (OCCR) and dark count rate with various bias currents at the wavelength of interests (1536nm). The input laser power is -96 dBm for the OCCR measurements and the results are shown in Fig. 2(e). When we biased both SNSPDs at 6 μA , the dark count rate of them are $0.22 \pm 0.06 \text{ Hz}$ and $0.07 \pm 0.03 \text{ Hz}$. The recovery time extracted from an exponential fitting is about 3.51 ns (see Supplementary Information), corresponding to a potential maximum count rate of about 280 MHz. For details of the SNSPDs, see Supplementary Information.

To benchmark the indistinguishability of the pulses along with the integrated chip of the relay server, we measure the two-photon Hong-Ou-Mandel (HOM) interference. This is realized by adjusting the relative electronic delay between Alice's and Bob's electrical pulses. As shown in Fig. 2(a), Alice and Bob each employs a CW laser (LS), and chops out early ($|0\rangle$) or/and late ($|1\rangle$) temporal modes by using intensity modulator (IM). This generates time-bin qubits with 426 ps duration and separated by 2 ns with a 100 MHz repetition rate. Then we send both pulses onto the chip and make coincidence counts measurement. As shown in Fig. 3(a), we obtain a HOM interference visibility of $V=48\% \pm 2\%$, which is calculated by $V = (CC_{max} - CC_{min})/CC_{max}$. CC_{max} and CC_{min} represent the maximum and minimum coincidence counts. These results

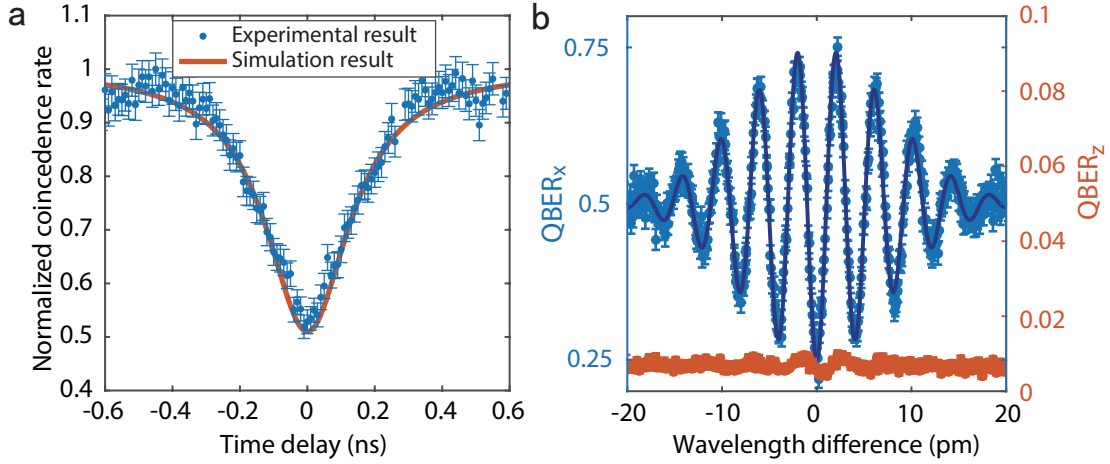


FIG. 3: (a) Hong-Ou-Mandel (HOM) interference as a function of relative electronic delays between Alice and Bob. A HOM interference visibility of $V = 48\% \pm 2\%$ is observed, which agrees well with the theoretical maximum value of 50%. By fitting the data with Lorentzian function, pulse width $\Gamma = 0.426$ ns. (b) Measured quantum bit error rate (QBER) in X-basis and Z-basis as a function of the relative wavelength detuning between two lasers. See text for details.

indicate the high quality of our integrated chip for MDI-QKD. The blue solid circles are experimental results and the red curve is a fit with Lorentzian function with a width about 426 ps. The visibility slightly deviates from the perfect theoretical prediction (50% for weak coherent pulses) is due to the residual difference of spectral modes, the finite extinction ratio (about 21.9 dB) of IMs. In order to perform long-time measurements, we reduced the bias current of SNSPDs, which correspondingly lower the performance of them.

After obtaining the high-visibility HOM interference, we proceed to the realization of MDI-QKD. We encode the information into the time-bins in Z-basis and X-basis. In Z-basis, the time-bins are 01 and 10 for bit values of 0 and 1, respectively. In X-basis, the time-bins are 11 with relative phases of 0 or π , representing bit values of 0 and 1, respectively. In experiment, we obtain secure keys from Z-basis encoding and verify the reliability of the setup in X-basis [16]. In Fig. 3(b), we show the measured quantum bit error rate (QBER) in X-basis ($QBER_x$, blue) and Z-basis ($QBER_z$, red). In the measurement of $QBER_x$, the two detection events are separated by t (2.9 ns, double the pulse width plus 2 ns separation), then the phase difference induced by frequency difference is

$$\theta = 2\pi(\omega_a - \omega_b)t = 2\pi t(\Delta\omega) = 2\pi t c \frac{|\lambda_a - \lambda_b|}{\lambda_a \lambda_b}, \quad (1)$$

where c is the speed of light, ω_a (ω_b) and λ_a (λ_b) are the laser frequency and wavelength of Alice (Bob), respectively. Alice and Bob exchange their keys conditionally on Charlie obtaining $|\Psi^-\rangle$ from his BSM. When Alice and Bob send the same/orthogonal states, the probability of Charlie obtaining a coincidence at two subsequent time bins is $P^-(t_0, t_0 + t)$ ($P^+(t_0, t_0 + t)$):

$$P^\pm(t_0, t_0 + t) = 1 \pm V \exp[-\tau^2 (c \frac{|\lambda_a - \lambda_b|}{\lambda_a \lambda_b})^2] \cos \theta, \quad (2)$$

where t_0 and $t_0 + t$ are the arrival-time of photons travelling to the two SNSPDs. τ is the coincidence window (1.1 ns). The QBER in X-basis [9] is

$$QBER_x = \frac{P^-(t_0, t_0 + t)}{P^-(t_0, t_0 + t) + P^+(t_0, t_0 + t)}. \quad (3)$$

The experimental data agree well with the theoretical prediction. Ideally, $QBER_z$, should not depend on the wavelength difference. However, due to the limited extinction ratio of intensity modulations, we also observe a small interference effect in $QBER_z$ in our experiment.

In order to verify the suitability of our integrated relay server for long-distance MDI-QKD, we introduce balanced attenuations between Alice-Charlie and Bob-Charlie to simulate the loss caused by long standard fibres (loss 0.2 dB/km). Fig. 4 (a) and (b) show the QBERs for X-basis and Z-basis and the sifted key rate as functions of loss and equivalent fibre length. We set the

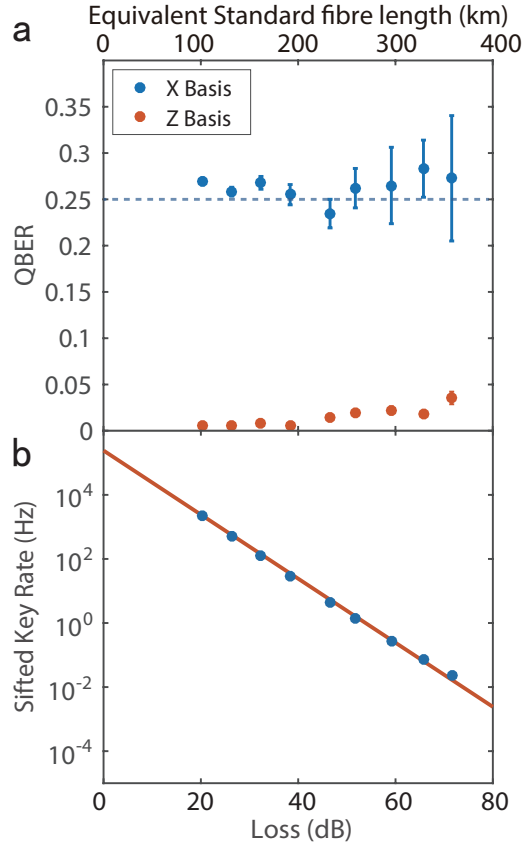


FIG. 4: (a) QBER for X-Basis and Z-Basis with various transmission losses. (b) Sifted key rates with different transmission loss are shown in blue solid circles and the simulation results are shown in red curve.

average photon number per pulse sent by Alice and Bob to be about 0.43 photon per pulse. The total loss includes losses from the simulated communication channel and grating couplers. The fiber-chip coupling loss is about 10.18 dB in the cryogenic environment, which is derived from reference ports. In Fig.4, each data point under different loss has collected for a time to ensure sifted key bits greater than 700. Our system generates 733 sifted bits in about 9 hours at 71.56 dB attenuation (equivalent to 357.8 km standard fiber) with $QBER_x=27\% \pm 7\%$ and $QBER_z=3.5\% \pm 0.7\%$, respectively. See SI for details. Note that our work is a proof-of-principle demonstration of MDI-QKD with an integrated relay server. Including decoy states and phase randomization as shown in previous work [11–18] will certainly improve the security and efficiency of the system.

In conclusion, we have demonstrated the first integrated relay server for MDI-QKD with a heterogeneous superconducting-silicon-photonic chip. The experimental high-visibility HOM interference and low QBER indicate that the integrated server is a promising platform for MDI-QKD. By using more advanced waveguide-integrated SNSPDs [29], one can further improve the integrated server with high detection efficiency, low timing jitter, and high repetition rate. Combined with photonic chip transmitters [32, 33], a full chip-based scalable MDI-QKD system should be realized in the near future.

Acknowledgements

This research is supported by the National Key Research and Development Program of China (2017YFA0303700, 2019YFA0308704), National Natural Science Foundation of China (Grant No. 11674170, 11690032, 11621091), NSFC-BRICS (No. 61961146001), NSF Jiangsu Province (No. BK20170010), the program for Innovative Talents and Entrepreneur in Jiangsu, and the Fundamental Research Funds for the Central Universities.

-
- [1] H.-K. Lo and H. F. Chau, *Science* **283**, 2050 (1999).
- [2] N. Gisin, G. Ribordy, W. Tittel, and H. Zbinden, *Rev. Mod. Phys.* **74**, 145 (2002).
- [3] V. Scarani, H. Bechmann-Pasquinucci, N. J. Cerf, M. Dušek, N. Lütkenhaus, and M. Peev, *Rev. Mod. Phys.* **81**, 1301 (2009).
- [4] F. Xu, X. Ma, Q. Zhang, H.-K. Lo, and J.-W. Pan, p. Preprint at <https://arxiv.org/abs/1903.09051> (2019) (????).
- [5] V. Makarov, A. Anisimov, and J. Skaar, *Phys. Rev. A* **74**, 022313 (2006).
- [6] Y. Zhao, C.-H. F. Fung, B. Qi, C. Chen, and H.-K. Lo, *Phys. Rev. A* **78**, 042333 (2008).
- [7] L. Lydersen, C. Wiechers, C. Wittmann, D. Elser, J. Skaar, and V. Makarov, *Nat. Photon.* **4**, 686 (2010).
- [8] M. Elezov, R. Ozhegov, G. Goltsman, and V. Makarov, *Opt. Express* **27**, 30979 (2019).
- [9] H.-K. Lo, M. Curty, and B. Qi, *Phys. Rev. Lett.* **108**, 130503 (2012).
- [10] A. Rubenok, J. A. Slater, P. Chan, I. Lucio-Martinez, and W. Tittel, *Phys. Rev. Lett.* **111**, 130501 (2013).
- [11] Y. Liu, T.-Y. Chen, L.-J. Wang, H. Liang, G.-L. Shentu, J. Wang, K. Cui, H.-L. Yin, N.-L. Liu, L. Li, et al., *Phys. Rev. Lett.* **111**, 130502 (2013).
- [12] Y.-L. Tang, H.-L. Yin, S.-J. Chen, Y. Liu, W.-J. Zhang, X. Jiang, L. Zhang, J. Wang, L.-X. You, J.-Y. Guan, et al., *Phys. Rev. Lett.* **113**, 190501 (2014).
- [13] Z. Tang, Z. Liao, F. Xu, B. Qi, L. Qian, and H.-K. Lo, *Phys. Rev. Lett.* **112**, 190503 (2014).
- [14] C. Wang, X.-T. Song, Z.-Q. Yin, S. Wang, W. Chen, C.-M. Zhang, G.-C. Guo, and Z.-F. Han, *Phys. Rev. Lett.* **115**, 160502 (2015).
- [15] L. Comandar, M. Lucamarini, B. Fröhlich, J. Dynes, A. Sharpe, S.-B. Tam, Z. Yuan, R. Pentz, and A. Shields, *Nat. Photon.* **10**, 312 (2016).
- [16] H.-L. Yin, T.-Y. Chen, Z.-W. Yu, H. Liu, L.-X. You, Y.-H. Zhou, S.-J. Chen, Y. Mao, M.-Q. Huang, W.-J. Zhang, et al., *Phys. Rev. Lett.* **117**, 190501 (2016).
- [17] C. Wang, Z.-Q. Yin, S. Wang, W. Chen, G.-C. Guo, and Z.-F. Han, *Optica* **4**, 1016 (2017).
- [18] H. Liu, W. Wang, K. Wei, X.-T. Fang, L. Li, N.-L. Liu, H. Liang, S.-J. Zhang, W. Zhang, H. Li, et al., *Phys. Rev. Lett.* **122**, 160501 (2019).
- [19] B. Fröhlich, J. F. Dynes, M. Lucamarini, A. W. Sharpe, Z. Yuan, and A. J. Shields, *Nature* **501**, 69 (2013).
- [20] R. J. Hughes, J. E. Nordholt, K. P. McCabe, R. T. Newell, C. G. Peterson, and R. D. Somma, p. Preprint at <https://arxiv.org/abs/1305.0305> (2013).
- [21] Y.-L. Tang, H.-L. Yin, Q. Zhao, H. Liu, X.-X. Sun, M.-Q. Huang, W.-J. Zhang, S.-J. Chen, L. Zhang, L.-X. You, et al., *Phys. Rev. X* **6**, 011024 (2016).
- [22] Y. Ding, D. Bacco, K. Dalgaard, X. Cai, X. Zhou, K. Rottwitt, and L. K. Oxenløwe, *Npj Quantum Inf.* **3**, 25 (2017).
- [23] D. Bunandar, A. Lentine, C. Lee, H. Cai, C. M. Long, N. Boynton, N. Martinez, C. DeRose, C. Chen, M. Grein, et al., *Phys. Rev. X* **8**, 021009 (2018).
- [24] C. Ma, W. D. Sacher, Z. Tang, J. C. Mikkelsen, Y. Yang, F. Xu, T. Thiessen, H.-K. Lo, and J. K. Poon, *Optica* **3**, 1274 (2016).
- [25] P. Sibson, J. E. Kennard, S. Stanisic, C. Erven, J. L. O'Brien, and M. G. Thompson, *Optica* **4**, 172 (2017).
- [26] P. Sibson, C. Erven, M. Godfrey, S. Miki, T. Yamashita, M. Fujiwara, M. Sasaki, H. Terai, M. G. Tanner, C. M. Natarajan, et al., *Nat. Commun.* **8**, 13984 (2017).
- [27] C.-Y. Wang, J. Gao, Z.-Q. Jiao, L.-F. Qiao, R.-J. Ren, Z. Feng, Y. Chen, Z.-Q. Yan, Y. Wang, H. Tang, et al., *Opt. Express* **27**, 5982 (2019).
- [28] G. Zhang, J. Haw, H. Cai, F. Xu, S. Assad, J. Fitzsimons, X. Zhou, Y. Zhang, S. Yu, J. Wu, et al., *Nat. Photon.* pp. 1–4 (2019).
- [29] W. H. Pernice, C. Schuck, O. Minaeva, M. Li, G. Goltsman, A. Sergienko, and H. Tang, *Nat. Commun.* **3**, 1325 (2012).
- [30] B. A. Korzh, Q.-Y. Zhao, S. Frasca, J. P. Allmaras, T. M. Autry, E. A. Bersin, M. Colangelo, G. M. Crouch, A. E. Dane, T. Gerrits, et al., p. Preprint at <https://arxiv.org/abs/1804.06839> (2018).
- [31] S. Ferrari, C. Schuck, and W. Pernice, *Nanophotonics* **7**, 1725 (2018).
- [32] H. Semenenko, P. Sibson, A. Hart, M. G. Thompson, J. G. Rarity, and C. Erven, p. Preprint at <https://arxiv.org/abs/1908.08745> (2019).
- [33] K. Wei, W. Li, H. Tan, Y. Li, H. Min, W.-J. Zhang, H. Li, L. You, Z. Wang, X. Jiang, et al., p. Preprint at <https://arxiv.org/abs/1911.00690> (2019).
- [34] O. Kahl, S. Ferrari, V. Kovalyuk, G. N. Goltsman, A. Korneev, and W. H. Pernice, *Sci. Rep.* **5**, 10941 (2015).
- [35] Y. Luo, Z. Nong, S. Gao, H. Huang, Y. Zhu, L. Liu, L. Zhou, J. Xu, L. Liu, S. Yu, et al., *Opt. Lett.* **43**, 474 (2018).

SUPPLEMENTARY INFORMATION

I. The heterogeneous superconducting-silicon-photonic chip for relay server.

In this section, we introduce the fabrication and characterization of the heterogeneous superconducting-silicon-photonic chip for relay server, which includes high-efficiency grating coupler (a) and waveguide-integrated superconducting nanowire single-photon detector (SNSPD) (b).

(a) Fabrication and performance of high-efficiency grating coupler

The fabrication steps of the high-efficiency grating coupler are shown in Fig. 5.

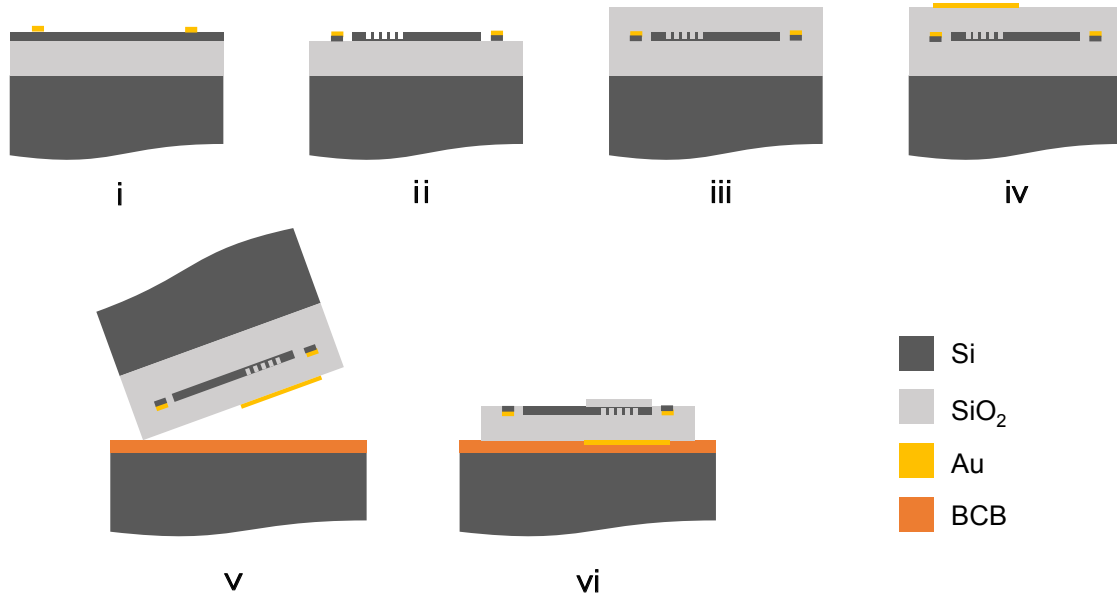


FIG. 5: Six-step fabrication process to realize the high-efficiency grating coupler. (i) The device is fabricated on a commercial Silicon-on-Insulator (SOI) wafer with $3\ \mu\text{m}$ thick buried oxide layer and $220\ \text{nm}$ thick top silicon layer. We fabricate gold pattern as the alignment markers for the subsequent steps. (ii) Silicon photonics structures (including waveguides, MMIs and grating couplers) are patterned by Electron Beam Lithography (EBL) and etched by the Inductively Coupled Plasma (ICP) etching process. (iii) A thickness of $3\ \mu\text{m}$ SiO_2 cladding is then deposited via the plasma-enhanced chemical vapor deposition (PECVD) and planarized via chemical mechanical polishing (CMP) to an optimized thickness. (iv) Gold reflectors are then defined by lithography, metal evaporation and lift-off processes on the SiO_2 cladding right above the grating couplers. (v) The chip is then flip-bonded to a silicon carrier wafer using benzocyclobuten (BCB). (vi) Finally, silicon substrate of the chip is removed by mechanical grinding and chemical etching, followed by dry etching the buried oxide layer.

Fig. 6 shows the transmission spectrum of the grating coupler with an insertion loss of about 1.05 dB, which allows us for optimizing future devices.

(b) Fabrication and performance of waveguide integrated SNSPD

The fabrication steps of waveguide integrated SNSPD are shown in Fig. 7 and explained in its caption. We use the setup in Fig. 8 to test the performance of the SNSPD, including its critical temperature, critical current, on-chip count rate (OCCR) and dark count rate (DCR) in closed-cycle fridge. In the electrical readout circuit, 2400 source meter provides a voltage source and a $100\ \text{k}\Omega$ resistor in series. Bias Tees (Minicircuit ZFBT4R2GW+) allow us to give a bias current to detector and get the response signal of the detector. The signal is amplified by an amplifier (MITEQ-1309), whose bandwidth is $1\ \text{kHz}\sim 1\ \text{GHz}$ and gain is 50 dB. Our sample is glued on the sample stage which is made from gold-plated oxygen-free copper. The sample stage is mounted on 3-axis closed-loop low-temperature piezo nanopositioner (Attocube). With the help of the nanopositioners, light can be coupled into the chip from SMF and fiber array. On the opposite side of fibre array, a RF probe (Cascade) is used to obtain the detectors' response signal.

Before we cooling down our sample, we have performed room-temperature (RT) measurement to characterize the quality of NbN nanowires using a probe station. In Fig. 9, we show the measured resistance for wires with different widths and lengths, in which the black, red and blue squares represent the RT resistances for wires with $100\ \mu\text{m}$, $80\ \mu\text{m}$ and $40\ \mu\text{m}$ lengths. The widths of the wires vary from $60\ \text{nm}$ to $100\ \text{nm}$ in $10\ \text{nm}$ step. The black, red and blue curves represent a theoretical calculation

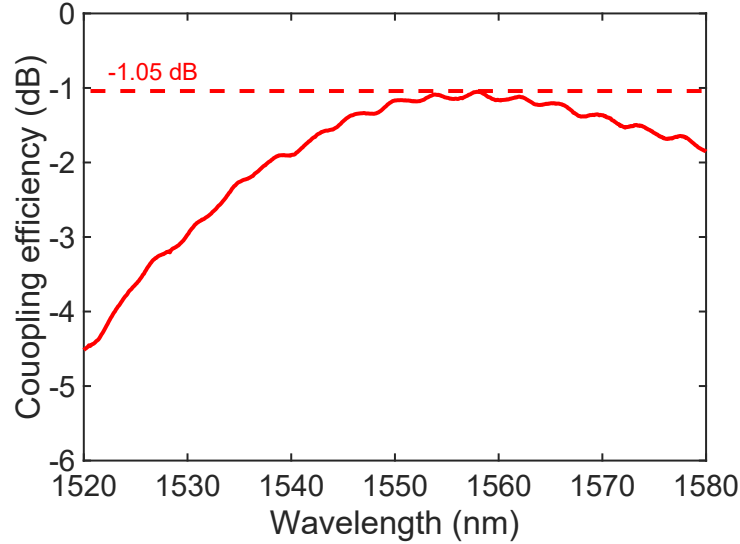


FIG. 6: Characterizations of coupling efficiency as a function of wavelength for the grating coupler with a bonded metal mirror before the nanowire fabrication. A peak coupling efficiency of -1.05 dB is observed.

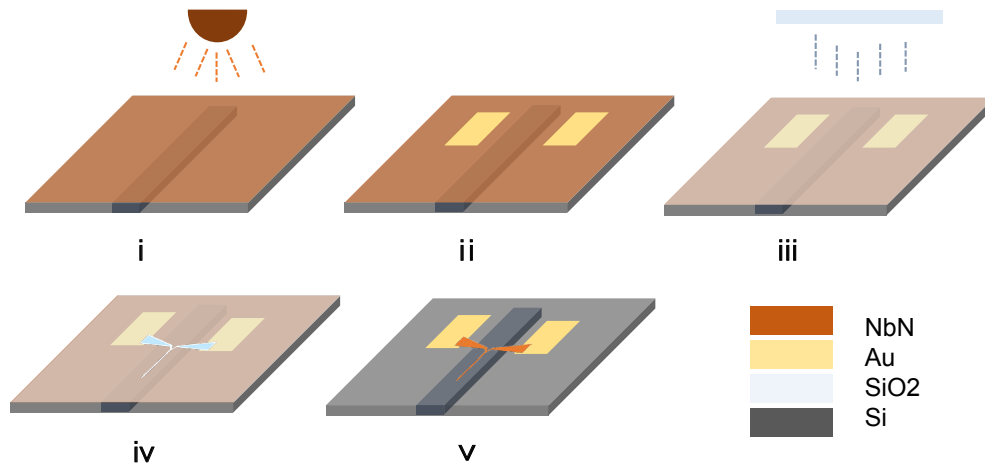


FIG. 7: **Fabrication of NbN based SNSPDs.** (i) A nominal 6nm NbN film is deposited on the chip by DC reactive magnetron sputtering. (ii) A standard lift-off process, including electron beam lithography (EBL), Ti and Au deposition and lift-off, is used to fabricate gold pads for electronic contacts. (iii) A 10 nm SiO₂ layer is deposited on NbN film by plasma-enhanced chemical vapor deposition (PECVD) to improve the adhesion between 2% hydrogen silsesquioxane (HSQ) and NbN [1]. (iv) Then, the detector pattern is defined by EBL and developed using 2.38% TMAH. (v) Lastly, SiO₂ and the unwanted NbN are etched away in a timed reactive ion etching (RIE) step with CF₄ plasma.

with a sheet resistance of $R_s=275 \Omega/\square$, which is obtained by a four-point probe measurement. The critical temperature of the wire is about 5.2 K.

After cooling the sample stage temperature down to 2.2 K, we perform further low-temperature measurements, such as critical current, temporal response, OCCR and DCR. In Fig. 10(a), the I-V curves are measured by sweeping the voltage source between -1 V and 1 V, connected with a 100 k Ω resistor. Each nanowire exhibits a superconducting state along the zero-voltage and abruptly transit to a normal-conducting state once the current is higher than critical current. It is clear to see that as the width of nanowire increases, the critical current increases. In Fig. 10(b), we obtain the pulse shape using an oscilloscope (Agilent Infiniium 54855A, bandwidth 6 GHz, 20 GSa/s). The data is averaged 64 times. The averaged transient amplified response pulses of an SNSPD with 60 nm-wide, 80 μm -long biased at 7 μA is exponentially fitted, giving an estimate of 3.51 ns for the $1/e$ -decay time.

The OCCR and DCR of SNSPD are characterized by input an attenuated continuous wave (CW) laser. A fiber polarization

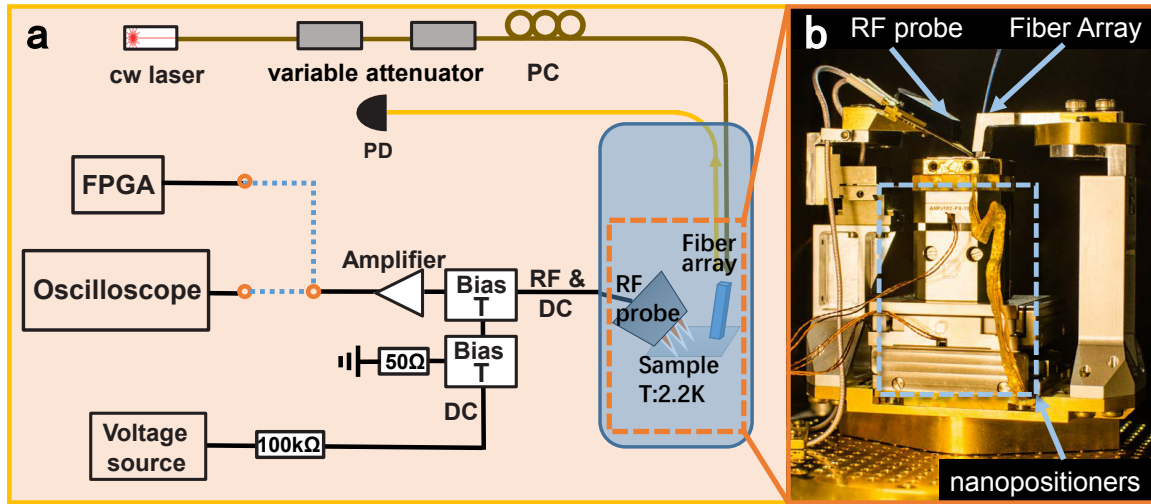


FIG. 8: (a) Setup for resistance, critical current, critical temperature, OCCR, and DCR measurements. See the text for details. (b) Photograph of sample stage which is mounted on a 3-axis closed-loop nano-positioner.

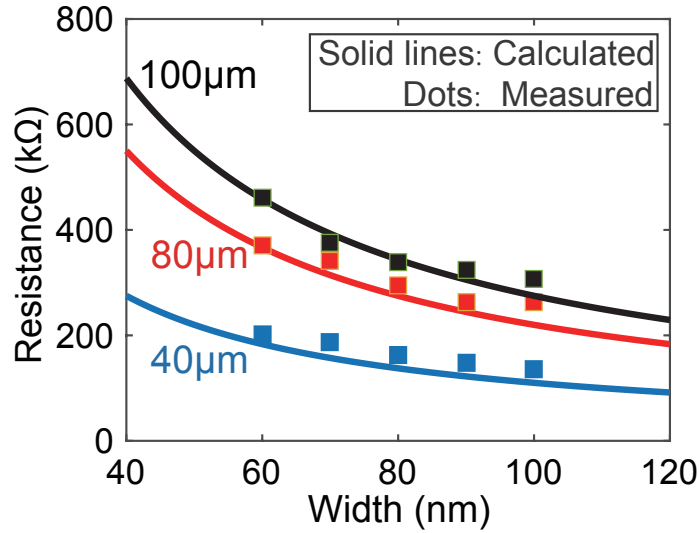


FIG. 9: Measured room temperature resistances for different nanowire geometries. The solid lines are theoretical predictions with a sheet resistance of $R_s=275 \Omega/\square$ at 300 K obtained by four-point probe measurement.

controller is used to maximize the input power. First, we characterize the coupling efficiency of the grating coupler. After the photon flux is guided to fiber array in the cryostat, we measure the input power P_{in} and output power P_{out} with the attenuator is set at 0 dB. The efficiency of the grating coupler can be calculated by the following formula

$$\eta_{in} * r * r * \eta_{out} = \frac{P_{out}}{P_{in}}, \quad (4)$$

where η_{in} and η_{out} is the efficiency of the grating coupler. We assume $\eta_{in} = \eta_{out} = \eta$ and neglect the on-chip propagation loss. r is the splitting ratio of MMI. We assume that the splitting ratio of multi-mode interference (MMI) is 50:50 in the following calculation. By adjusting the attenuator, we can find the photon number N arriving at the detector in a similar way, with

$$N = \frac{P_{in}}{h\nu} * \eta * r * r. \quad (5)$$

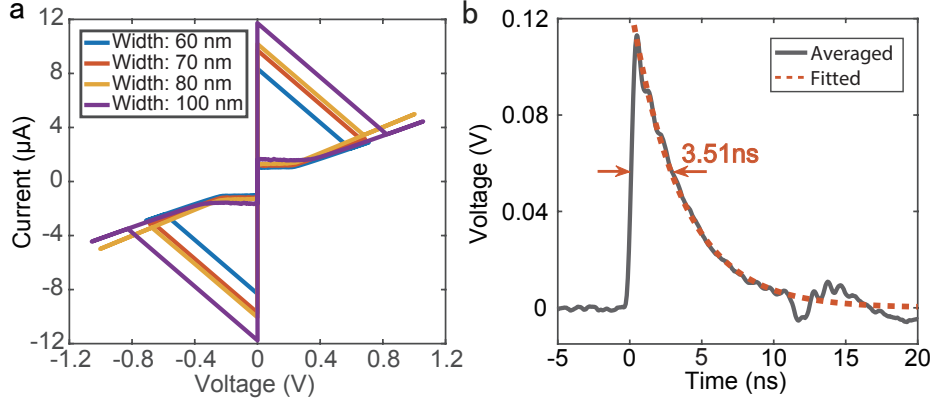


FIG. 10: (a) I-V curves of 4 nanowires with different widths. (b) The averaged transient amplified response pulses of an SNSPDs with 60nm-wide, 80 μm -long biased at 7 μA . Exponential fits reveal the $1/e$ -decay times are 3.51 ns.

When the attenuation is A , with $N_{in} = N * A$, the on-chip detection efficiency (OCDE) can be written as

$$OCDE = \frac{C - C_d}{N_{in}}, \quad (6)$$

where C is OCCR and C_d is DCR. We can get the value of C and C_d by using FPGA unit to timetag the data. DCR is the count per second when we turn off the laser. We change the bias current of our SNSPD and obtain the OCCR and DCR curve as a function of bias current (see Fig. 2e in the main text). From these analysis, we obtain a OCDE of about 52% at a bias current of 6 μA .

II. Off-chip optical setup.

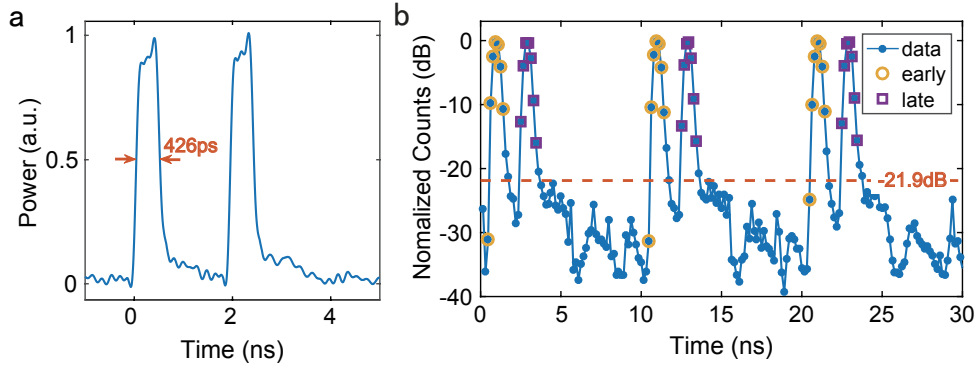


FIG. 11: (a) Normalized waveform of the experimentally chopped X-basis optical pulses with a separation of 2 ns. The pulse train is detected by a 40 GHz photodetector with the waveforms obtained by a 20 GHz sampling oscilloscope. The full width at half maximum (FWHM) of the pulses is 426 ps. (b) Histogram of the weak coherent pulse train (less than one photon per pulse) with a rate of 100 MHz is detected by the waveguide integrated superconducting nanowire single-photon detector (SNSPD). The extinction ratio of the pulses is more than 21.9 dB. The detector electrical signals are collected by a field-programmable gate array (FPGA)-based timetag device with a bin resolution of 156 ps. We select a time window of 7 bins for the early and late temporal modes (denoted as yellow and purple circles in the figure).

In our experiment, the light sources are two CW lasers with a linewidth of 100 Hz centered at 1536.47 nm. Then we use intensity modulators to chop out the required short pulses with about 426 ps full-width at half maximum (FWHM). The separation between two pulses in X-basis is about 2 ns. The results of high-intensity light measured with 40 GHz photodetector are

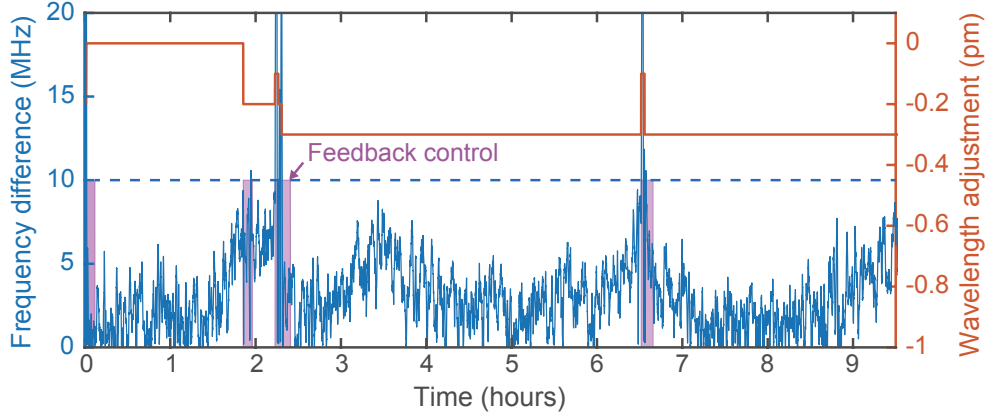


FIG. 12: Frequency difference between the lasers of Alice and Bob with the feedback signal coming from beat measurement for about 9.5 hours, during which a maximum frequency drift no more than 10 MHz is observed. The purple areas are the working time of the feedback system and the brown line indicates the value of the wavelength adjustment with a resolution of 0.1 μm .

shown in Fig. 11(a). We show the results of weak coherent pulses measured with our SNSPDs in Fig. 11(b), in which a 21.9 dB extinction ratio has been obtained in the single-photon counting regime.

For our experiment, it is important to keep the frequencies of both Alice and Bob's lasers to be the same. We keep track on the frequency difference between these two lasers and employ a feed-back system to regulate Bob's laser's frequency. The maximum frequency difference is less than 10 MHz over about 9.5 hours with the help of the feed-back system, as shown in Fig. 12.

III. Experimental results.

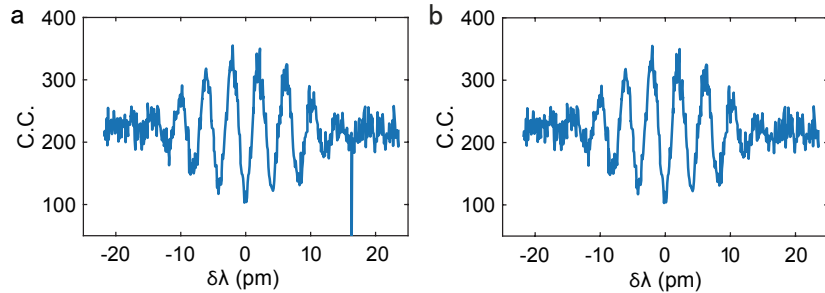


FIG. 13: Raw (a) and post-processed (b) coincidence counts (C.C) between two detectors at two subsequent time bins as a function of the relative wavelength difference between Alice and Bob when both Alice and Bob send $|+\rangle$ state. The average photon number per pulse is about 0.43 and the integration time for each data is 5 seconds. The abrupt change of C.C to zero in raw data (a) is due to the imperfection of the read-out circuitry causing a switching of the nanowire from superconducting to a normal-conducting state. The count is zero in this case. In (b), we removed this data point.

In Fig. 13(a), we show a typical experimental result we obtained with X-basis encoding. Note that the sudden change of C.C to zero (close to 18 μm) in raw data (a) is due to the imperfection of the electron circuitry causing a switching of the nanowire from superconducting to a normal-conducting state. The count is zero in this case. In (b), we removed this data point. A better voltage source and read-out circuitry could prevent this to happen, which we are working on now.

In Fig. 14, we show the full post-processed coincidence counts between two detectors at two alternative times as a function of the relative wavelength between Alice and Bob for randomly chosen time-bin states.

In Table I, we show the complete results of the sifted keys under different attenuations, along with the Z-basis sifted key rate (SKR), quantum bit error rate in Z- ($QBER_z$) and X- ($QBER_x$) bases and their corresponding error bars ($QBER_z$ errorbar

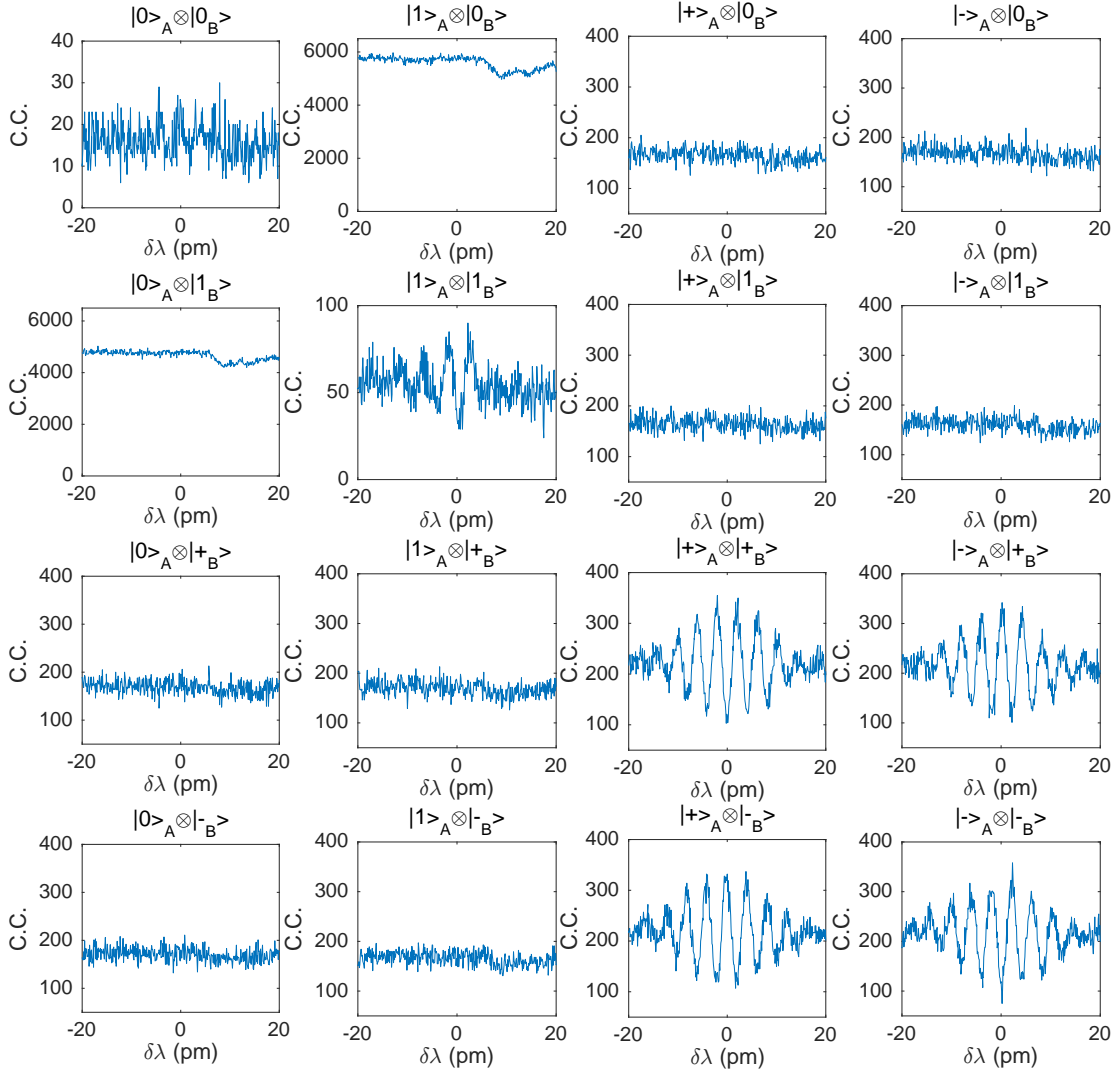


FIG. 14: Full post-processed C.C between two detectors at two alternative times as a function of the wavelength difference between Alice and Bob for randomly chosen time-bin states.

and $QBER_x$ errorbar).

TABLE I: List of experimental results under different attenuations

| Time (s) | Att (dB) | Sifted key (bits) | SKR(bits/s) | $QBER_z$ | $QBER_z$ error bar | $QBER_x$ | $QBER_x$ error bar |
|----------|----------|-------------------|-------------|----------|--------------------|----------|--------------------|
| 90 | 20.36 | 193414 | 2.15E+03 | 0.58% | 0.02% | 26.9% | 0.3% |
| 190 | 26.36 | 99286 | 5.23E+02 | 0.62% | 0.02% | 25.8% | 0.5% |
| 390 | 32.36 | 50722 | 1.30E+02 | 0.77% | 0.04% | 26.8% | 0.7% |
| 620 | 38.36 | 18415 | 2.97E+01 | 0.62% | 0.06% | 26% | 1% |
| 1920 | 46.56 | 8547 | 4.45E+00 | 1.5% | 0.1% | 23% | 2% |
| 3900 | 51.76 | 5320 | 1.36E+00 | 1.9% | 0.2% | 26% | 2% |
| 4860 | 59.16 | 1266 | 2.60E-01 | 2.2% | 0.4% | 26% | 4% |
| 32880 | 65.76 | 2348 | 7.14E-02 | 1.8% | 0.3% | 28% | 3% |
| 32280 | 71.56 | 733 | 2.27E-02 | 3.5% | 0.7% | 27% | 7% |

[1] Kahl, O. *et al.* Waveguide integrated superconducting single-photon detectors with high internal quantum efficiency at telecom wave-lengths. *Sci. Rep.* **5**, 10941 (2015).